

Space Weather®



RESEARCH ARTICLE

10.1029/2021SW003012

Key Points:

- New soft X-ray photoelectron model is used with solar flare models as input to atmospheric chemistry models
- Comparison with E region radar data is consistent with enhanced flux in the 1-2 nm solar spectral region
- D region comparisons show agreement with observed HF absorption, but large disagreement with very low frequency data

Correspondence to:

D. E. Siskind, david.siskind@nrl.navy.mil

Citation:

Siskind, D. E., Jones, M., Jr., Reep, J. W., Drob, D. P., Samaddar, S., Bailey, S. M., & Zhang, S.-R. (2022). Tests of a new solar flare model against D and E region ionosphere data. *Space Weather*, 20, e2021SW003012. https://doi.org/10.1029/2021SW003012

Received 14 DEC 2021 Accepted 10 MAR 2022

Author Contributions:

Conceptualization: David E. Siskind Data curation: Shun-Rong Zhang Formal analysis: David E. Siskind, Srimoyee Samaddar

Funding acquisition: David E. Siskind Investigation: David E. Siskind, McArthur Jones, Jeffrey W. Reep, Doug P. Drob

Methodology: David E. Siskind, McArthur Jones, Jeffrey W. Reep, Srimovee Samaddar

Project Administration: David E. Siskind

Resources: Scott M. Bailey

Software: David E. Siskind, Doug P. Drob, Scott M. Bailey

Supervision: David E. Siskind, Scott M. Bailey

Validation: David E. Siskind Visualization: David E. Siskind

© 2022. The Authors. Space Weather published by Wiley Periodicals LLC on behalf of American Geophysical Union. This is an open access article under the terms of the Creative Commons Attribution License, which permits use, distribution and reproduction in any medium, provided the original work is properly cited.

Tests of a New Solar Flare Model Against D and E Region Ionosphere Data

David E. Siskind¹, McArthur Jones Jr.¹, Jeffrey W. Reep¹, Doug P. Drob¹, Srimoyee Samaddar², Scott M. Bailey², and Shun-Rong Zhang³

¹Space Science Division, Naval Research Laboratory, Washington, DC, USA, ²Bradley Department of Electrical and Computer Engineering, Virginia Tech, Blacksburg, VA, USA, ³Massachusetts Institute of Technology Haystack Observatory, Westford, MA, USA

Abstract We present results from a suite of models designed to simulate solar flare effects on the D and E region of the ionosphere. This suite includes models of the solar spectrum, the ionosphere and of HF radiowave propagation. A central component of this system is the development of photoelectron ionization enhancement factors with higher energy resolution in the soft X-ray spectral region that can be used to supplement existing ionization schemes currently implemented in upper atmospheric general circulation models. We tested this photoelectron model in the NCAR Thermosphere-Ionosphere-Mesosphere-Electrodynamics General Circulation Model (TIME-GCM) and in a photochemical model of the D region. In both cases, we compared predicted flare response using two different input solar flare spectra. One is the Flare Irradiance Spectral Model (FISM) and the other is a physics based model called NRLFLARE. Our predictions for the E region were compared with incoherent scatter radar data and suggest that enhanced flux in the 1-2 nm spectral region, as indicated by NRLFLARE, is important for reproducing the observations. For the D region, we combined our theoretical results for the X1.3 flare of 7 September 2017 with ray tracing calculations that suggest 20-40 db of 6.4 MHz absorption. This agrees with previously published observations and model estimates, all of which suggest greater HF absorption than the operational D region absorption prediction model (swpc.noaa.gov/ products/d-region-absorption-predictions-d-rap). Finally, our theoretical comparison with previously published empirical models derived from very low frequency data was less clear due, in part, to large differences between the different empirical models.

Plain Language Summary Solar flares are of great interest for their effects on planetary ionospheres and radiowave propagation. Here we present a suite of models that can model flares and their terrestrial effects. We model the solar spectrum, the resulting ionization, the ionospheric consequences and the resulting effects on radiowave absorption. Our primary interest is in the ionospheric D and E regions (50–120 km altitude) which are ionized by the soft X-ray region (energies greater than about 500 keV) of the solar spectrum. Unfortunately, this wavelength region is not well characterized compared with the longer ultraviolet wavelengths. Further, because soft X-rays are so energetic, they produce most of their ionization not by primary photon ionization, but by secondary photoelectron impact. We compare two models of the solar spectrum and develop a new parameterization of photoelectron impact ionization to address these uncertainties. We then input these results into two different atmospheric models and compared to various previously published observations at different altitudes. Our results illustrate the key wavelength regions in the solar spectrum where more data is needed, specifically from 1 to 2 nm, and also highlight the need for new approaches toward measuring the response of the lowermost ionosphere to solar flares.

1. Introduction

The effect of a solar flare on the D and E region of the ionosphere has long been of interest for both practical and theoretical reasons. The practical reason for interest is the dramatic effect the flare induced changes in the ionosphere have on radiowave propagation at a wide range of frequencies. Flare effects have been studied using VLF propagation (McRae & Thomson, 2004; Thomson et al., 2005) and MF (Li et al., 2019) and HF (Davies, 1990; Eccles et al., 2005) frequencies as well as with incoherent scatter radars (Qian et al., 2019; Xiong et al., 2011) and GPS signals (Amaechi et al., 2021). Other studies have focused on how the enhanced ionization feeds back onto perturbations in ionospheric conductivity (Curto et al., 1994) and ionospheric currents (Grodji et al. (2022)).

SISKIND ET AL. 1 of 19



Writing – original draft: David E. Siskind Writing – review & editing: David E. Siskind, McArthur Jones, Jeffrey W. Reep, Scott M. Bailey, Shun-Rong Zhang The theoretical interest dates back to Nicolet and Aikin (1960) who noted that for the D region, during quiescent solar conditions, the dominant ionization would be from the lyman alpha ionization of nitric oxide; however, that "conditions due to solar flares must be explained by X-rays." Subsequent satellite observations of both lyman alpha and soft X-ray variability validated this hypothesis (Kreplin et al., 1962). There are several complications in modeling the D region response to solar flares. The first which has long been recognized (Mitra & Rowe, 1972) is that the photochemistry of the D region is extremely complex, comprising reactions with positive molecular ions, positive cluster ions, positive proton hydrates, negative molecular ions and finally, free electrons (Pavlov, 2014; Reid, 1977; Thomas & Bowman, 1985). The second modeling problem is that the shape of the solar spectrum in the soft X-ray region (defined here as wavelengths less than 5 nm) is poorly characterized. Finally, the dominant soft X-ray ionization mechanism is not from the primary photons, but from secondary photoelectrons (Woods et al., 2003). Extant models of soft X-ray induced photoelectron ionization effects on the D and E region that are used in physics based atmospheric models are typically highly parameterized and approximate (Fuller-Rowell, 1993; Sojka et al., 2013; Solomon & Qian, 2005). Solomon and Qian (2005) provide a discussion of the difficulties of developing a physics based model of soft X-ray effects. Here we attempt to improve upon this situation in two ways. First, we use two newer solar spectral models, one empirical and one physics based, to characterize the soft X-ray spectrum. While these models do not necessarily always agree, taken together, they can constrain the problem and provide useful insights to guide future studies of the solar spectrum. Second, we present detailed photoelectron enhancement factors down to wavelengths below 0.1 nm that can supplement the existing Solomon and Qian (2005) table. Since the atmospheric absorption cross section varies dramatically across soft X-ray wavelengths (Henke et al., 1993), our new model will allow greatly improved altitude resolution of the effects of soft X-ray ionization deep into the lower ionosphere. We then apply these models to two physics based models of the ionosphere and then also calculate HF absorption effects.

The general outline of the paper is as follows. In Section 2 we describe the six models that we use to characterize the effects of solar flares on the Earth's ionosphere, starting with two models of the solar spectrum and ultimately ending up in the Earth's D and E regions where radiowave propagation is impacted. These models are applied to study five specific flares. In Section 3, we compare the ionospheric and radiowave calculations for these flares with observations from previously published incoherent radar, ionosonde and VLF data. Section 4 presents our conclusions and provides discussion of residual uncertainties.

2. Modeling Approach

Our approach is to combine six models of the solar flux, the atmosphere/ionosphere, and radio propagation to quantify the ionospheric D and E region response to solar flares. Of these six models, two provide representations of the solar spectrum, the well known Flare Irradiance Spectral Model (FISM, Chamberlin et al., 2020) and a newer physics-based model of coronal loops, NRLFLARE (Reep et al., 2021). We then introduce a new model of photoelectron production that that builds upon the Solomon and Qian (2005) parameterization and that uses the solar spectra to calculate ionization rates. These ionization rates are used as input to two well known ionospheric models, the NCAR Thermosphere-Ionosphere-Mesosphere-Electrodynamics General Circulation Model (NCAR TIME-GCM) (e.g., Jones et al., 2017; Roble & Ridley, 1994) which we use for E-region analysis and the OASIS (Originally Austrian Study of the Ionosphere) D region model (Siskind et al., 2017, 2018; Torkar & Friedrich, 1983). Finally, the calculated electron density profiles are input to the MOJO (Modified Jones) radiowave propagation code (Zawdie et al., 2017) Our new photoelectron model improves upon the existing solar flux models used by those two models in that it better resolves the soft X-ray region. Further, we can test the effects of using two models of the solar flux. This section describes the six models.

In describing these models, we will be presenting examples from the five flares that are summarized in Table 1. These flares will also be the basis for our comparisons with various datasets in Section 3. These five flares range in energy from M5 to X17, thus a factor of 34 in X-ray flux. Table 1 presents a variety of parameters related to these flares that we will refer to and explain in subsequent discussions. These parameters are: the flare dates, the peak minute of the flare, the sub solar longitude, two estimates of peak flux in the 0.1–0.15 nm spectral bin that we will discuss and two measures of very low frequency (VLF) propagation that we will also discuss later.

SISKIND ET AL. 2 of 19



Table 1 Summary of Flares for Model/Data Comparisons								
Date	Class	dB	Peak minute	Sub solar long.	Peak flux ¹	Peak flux ²	H' (Thomson)	H' (Singh)
7/23/16	M5	17.0	314	101E	2.94×10^{4}	6.79×10^{4}	62.7 km	68.6 km
9/07/17	X1.3	21.3	875	39W	1.33×10^{5}	2.20×10^{5}	60.2 km	67.5 km
8/09/11	X6.9	28.3	484	59E	3.50×10^{5}	1.42×10^{6}	56.2 km	63.7 km
9/10/17	X8.3	29.2	966	61W	8.47×10^{5}	1.26×10^6	55.7 km	63.1 km
9/07/05	X17	32.3	1069	87W	7.91×10^{5}	1.90×10^{6}	54.2 km	60.3 km
¹photons.cm=2s=1 for 0.1=0.15 nm from FISM ²same from NRI FI ARE								

2.1. Solar Flux

The standard solar flare model used in upper atmospheric studies, which we use here, is FISM. The original version of FISM (Chamberlin et al., 2008) was based upon data from the GOES, TIMED and UARS/SOLSTICE satellites. Recent publications using FISM include Qian et al. (2019) and Pettit et al. (2018). Most recently FISM V2.0 has been released (Chamberlin et al., 2020). Compared with the previous version, FISM2, takes advantage of new datasets such as the EUV Variability Experiment (EVE) on the Solar Dynamics Observatory (SDO) and a newer version of SOLSTICE from the SORCE satellite. In addition, FISM2 offers higher spectral resolution (0.1 vs. 1.0 nm for the older version). As with the older FISM V1.0 model, FISM2 provides both a daily background spectrum as well as a flare spectral estimate every minute; we use this cadence as input into the atmospheric models discuss below.

We also make use of the newly introduced NRLFLARE model (Reep et al., 2020, 2022), a physically derived model of the solar flare irradiance that combines a series of hydrodynamic simulations of flaring coronal loops to synthesize the emission as a function of time. NRLFLARE is driven by a series of hydrodynamic loop simulations that reproduce the observed GOES/XRS time series. The ratio of the two XRS channels approximates the temperature of the plasma, and so informs the heating rates of the simulations, while the magnitude of the emission approximates the total volume of the loop (see Warren, 2005 or Reep et al., 2020 for details). Each loop is a cylinder with a fixed length and variable cross section. There are a few major advantages to such a model: (a) we can test the physics of solar flares and magnetic reconnection, (b) we can produce spectra at any desired cadence or spectral resolution, (c) we can extrapolate to extreme events with physics rather than empirical estimates. The flip side of this is that a physical model requires all of the correct physical processes to be accounted for and treated accurately, and there are still many facets of flares that are not properly treated in detail. For example, Reep et al. (2022) shows that the cross-section of the flaring loops cannot be assumed to be uniform, as is generally done in the literature. In the spectra in this paper, we have applied a correction to the loop cross section that accounts for its variation with temperature as a result. Reep et al. (2022) showed that this correction yielded good agreement between NRLFLARE and EVE light curves.

Figure 1 shows a comparison of spectra from FISM2 to NRLFLARE (binned to 0.1 nm resolution) for the peak minute of three of the flares summarized in Table 1. These three flares will be the focus of more detailed comparisons with ionospheric data. The spectral region we use for comparison corresponds to those wavelengths which are absorbed in the ionosphere below 120 km. Furthermore, these wavelengths are where NRLFLARE's approach is most valid, since the model is only constrained by X-rays observed by GOES, forming at similarly high temperatures. To synthesize the spectral emission, we use the CHIANTI atomic database, v.10 (Delzanna et al., 2021; Dere et al., 1997), which can be used to calculate emissivities or spectra relevant to optically thin plasmas-a good approximation in the soft X-rays. The photon flux is presented on both a linear wavelength scale (left column) and a logarithmic wavelength scale (right column). This is to allow the reader to focus on different parts of the spectrum. There is a general but not universal tendency for NRLFLARE to predict greater emission than FISM. This is most evident for the two strongest flares (top two rows of Figure 1). What is interesting is that while NRLFLARE and FISM typically agree in the spectral shape, there are some regions where they disagree, most notably in the 1–2 nm region. The continuum in this wavelength region is dominated by thermal bremsstrahlung (free-free emission), and there are many lines from highly ionized iron, calcium, nickel, and oxygen, with log T > 6.9. Most notably, in the top two rows of Figure 1, we see that from 1.2 to 1.8 nm, FISM shows a dip and

SISKIND ET AL. 3 of 19



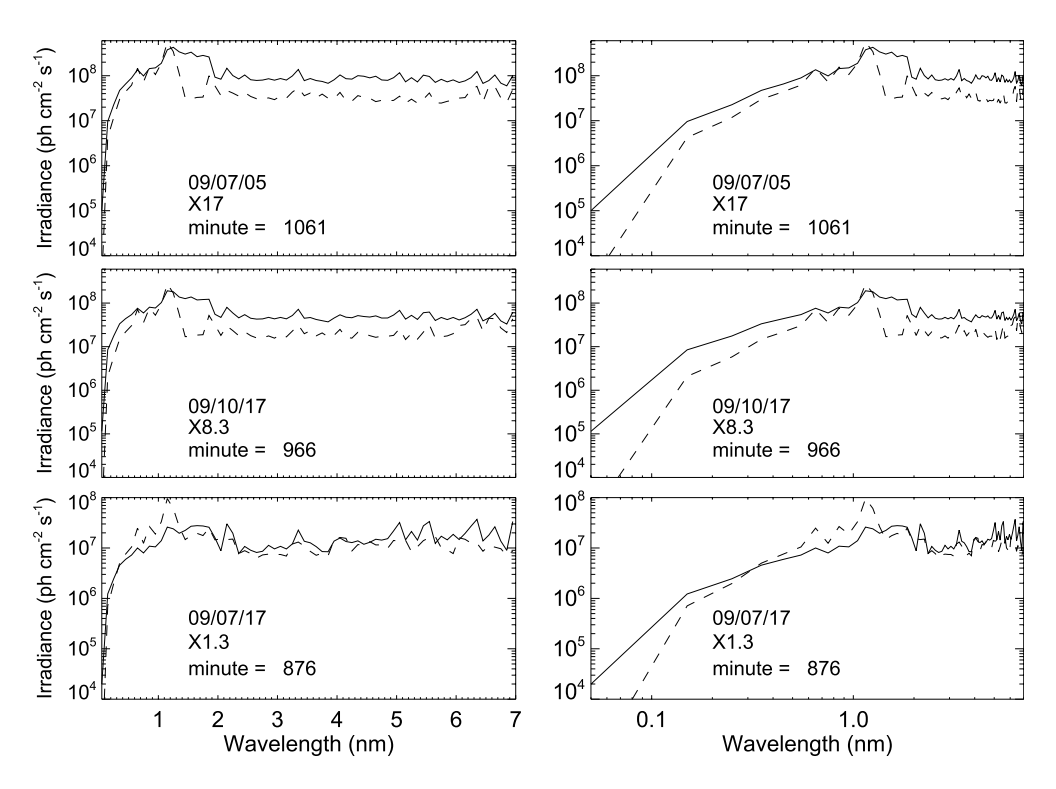


Figure 1. Comparison of NRLFLARE (solid) and FISM 2.0 (dashed) spectra for near the peak minute of the three flares indicated. The left and right columns are identical except for how the wavelength scale is plotted. *Note*. The order of magnitude difference in the flux between NRLFLARE and FISM in the 1–2 nm region for the X8.3 and X17 flares.

NRLFLARE shows an enhancement such that the total photon flux in this region is about an order of magnitude greater in NRLFLARE relative to FISM. Although spectral data for this wavelength region is limited, and only sparsely covered with modern instrumentation, there is an older spectrum by Neupert et al. (1967, see their Figure 2), taken from the Orbiting Solar Observatory (OSO) that shows numerous bright iron lines in the 1–1.8 nm region during a flare and overall looks more similar to NRLFLARE than to FISM. Siskind et al. (1995) have documented the importance of this wavelength region for calculations of lower thermospheric nitric oxide. In Section 3.1 below, we will show the consequences of this wavelength region for the calculated E region electron density response to flares. For the Sept 7, 2017 X1.3 flare the dip in FISM is not seen and the agreement with NRLFLARE here is generally good. On the other hand, in the 0.6–1.0 nm region for this flare, FISM predicts greater photon flux than NRLFLARE. Finally, for all three flares at the very shortest wavelengths (<0.4 nm), NRLFLARE consistently predicts greater flux than FISM. As we will show below, we will be able to directly relate these differences in predicted photon flux to differences in calculated radio wave absorption.

Figure 2 shows the evolution of the X17 2005 flare as predicted by FISM and NRLFLARE for some specific wavelength bins. The bins will be further described in the section below. For now, the left hand column (shorter wavelengths) presents D region ionization and the right hand column presents wavelength bins relevant for the E region. Figure 2 highlights another difference between FISM and NRLFLARE, namely in the time evolution of the flare. In general, the two models agree better during the rising portion of the flare, but NRLFLARE decays much more slowly. Note the dramatic difference in the 1.4–1.8 nm bin where NRLFLARE is a factor of 5 greater than FISM at the peak of the flare according to FISM, but then is over an order of magnitude greater in the minutes afterward. Reep et al. (2022) examined the decay of 12 spectral lines measured with SDO/EVE and found good agreement with the time evolution in the model and observations, even though the intensity is often too high in the model.

2.2. Photoelectron Ionization

The importance of an accurate model of photoelectrons stems from the fact that, at soft X-ray wavelengths, most of the ionization is not from the primary photon, but from secondary ionization due to photoelectrons (Siskind

SISKIND ET AL. 4 of 19

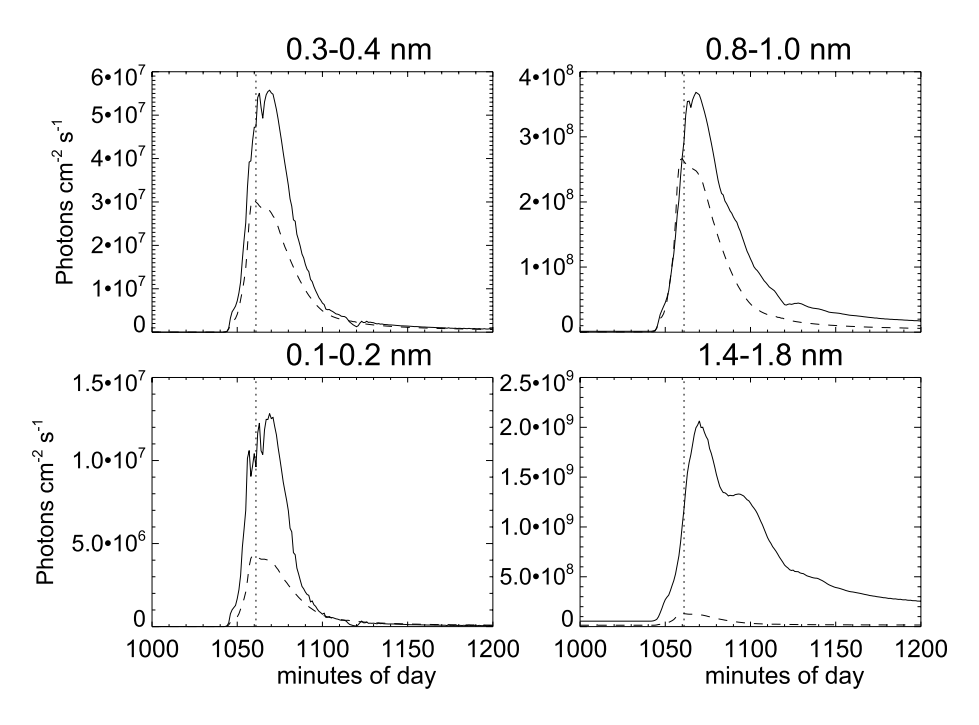


Figure 2. Time history of the modeled solar soft X-ray irradiance in 4 wavelength bins for the Sept 7, 2005 X17 flare. NRLFLARE output is solid, FISM is dashed. The dotted vertical line is a fiducial to mark the minute (1061) of the flare peak in FISM which was shown in Figure 1.

et al., 1990). Our approach to modeling photoelectron ionization follows the parameterization presented by Solomon and Qian (2005, hereinafter SQ05). They divided the solar spectrum into a number of bands characterized by an average cross section and an average photoelectron enhancement factor. They discuss the limitation that their spectral resolution at the shortest wavelengths is likely too coarse to adequately resolve the ionization at these wavelengths. For example, their shortest wavelength bin, from 0.05 to 0.4 nm, covers a factor of eight in energy. Since the N_2 cross section varies by about a factor of a 100 over this spectral band, such coarseness introduces

Table 2 *Cross Sections and Photoelectron Factors for N*,

bin no.	λ short, nm	λ long, nm	$\sigma_{abs} {\rm cm}^2$	p_{ρ}/p_{i} total		
			abs CIII	P _e P _i total		
First SQ05 band (0.05–0.4 nm)						
1	0.05	0.1	3.38×10^{-23}	554.2		
2	0.1	0.15	1.49×10^{-22}	312.1		
3	0.15	0.2	4.55×10^{-22}	219.0		
4	0.2	0.25	1.03×10^{-21}	168.3		
5	0.25	0.3	2.04×10^{-21}	136.9		
6	0.30	0.4	3.91×10^{-21}	108.7		
Second SQ05 band (0.4–0.8 nm)						
7	0.4	0.5	8.59×10^{-21}	83.2		
8	0.5	0.6	1.56×10^{-20}	67.4		
9	0.6	0.8	3.15×10^{-20}	53.2		
Third SQ05 band (0.8–1.8 nm)						
10	0.8	1.0	6.43×10^{-20}	40.7		
11	1.0	1.4	1.41×10^{-19}	30.8		
12	1.4	1.8	3.02×10^{-19}	22.5		

important uncertainties as to where the photons are absorbed and how much and where the ionization is produced. Here we present a modification of the SQ05 parameterization to address this limitation.

As SQ05 discuss, the coarseness of their model was driven by the general lack of information about the solar flux variation at soft X-ray wavelengths. Since SQ05, this lack of information has been partially ameliorated. First, as noted above, the revised FISM2 model now presents solar spectra at 0.1 nm resolution. Second, our physics based solar flare model, NRLFFLARE, can also be run at 0.1 nm, or even finer, spectral resolution. Thus we break out the three shortest wavelength SQ05 wavelength bands into a total of 12 finer sub-bands. Since the old SQ05 model has 37 bands (including the FUV) as configured in the NCAR general circulation models, we call our model the 46 bin model (12 new bands replacing the 3 shortwave SQ05 bands, thus 9 more). The cross sections and secondary photoelectron ionization for N_2 are given in Table 2 and serve as the basis for subsequent discussion.

To understand Table 2, Figure 3 presents an example of the calculated direct photoionization and photoelectron ionization for N_2 for the peak of the X8.3 flare of 10 September 2017. The solar flux uses FISM (middle panels of Figure 1) and the photoelectron ionization is based upon the two stream photoelectron code of Solomon et al. (2001) and Bailey et al. (2002) that has been implemented at Virginia Tech in the IDL computer language to serve both research and education purposes. Figure 3 shows examples of these rates

SISKIND ET AL. 5 of 19



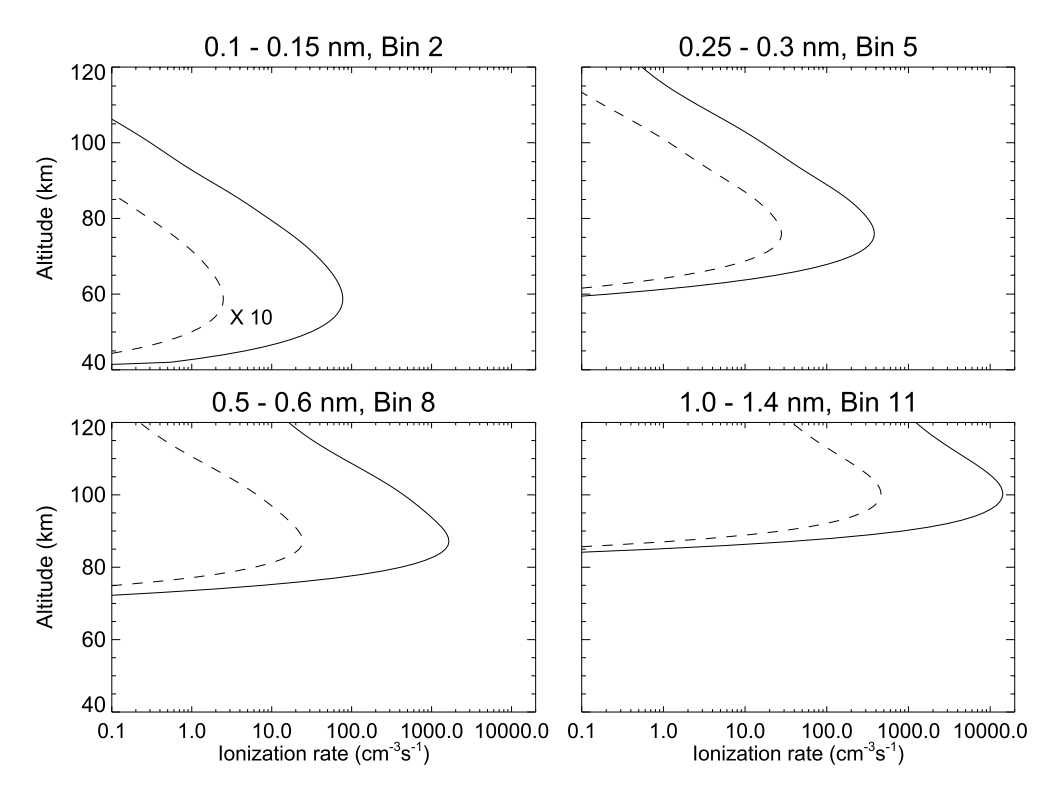


Figure 3. Sample N_2 photoionization (dashed) and photoelectron ionization (solid) rates for four wavelength bins using the FISM spectrum for the peak of the 10 September 2017 flare (middle panels of Figure 1). The photoionization for Bin 2 is multiplied by 10 to get it to appear on the same scale as the rest of the curves. Overhead sun is assumed.

for four of the bins listed in Table 2. It can be seen that as one moves to longer wavelengths, the ratio of the photoelectron to photoionization rates becomes smaller, reflecting the lower energy of the incident photon. Also, both the photoionization and photoelectron rates move up in altitude. This reflects the increasing N_2 absorption cross section seen in Table 2 (taken from Henke et al., 1993). The peak absorption occurs roughly at an optical depth of 1. This fact was used to guide the division into the 12 new sub-bands. Since the photon wavelength translates into the altitude of absorption in the atmosphere, the intent was to provide reasonable altitude resolution in the D and lower E regions, subjectively defined as about 4–6 km (also computational convenience was a consideration, i.e., wavelength boundaries on easily referenced numerical values).

Figure 4 illustrates this by plotting the optical depths for the 12 new bands as a function of altitude. Shown for reference is a vertical line marking a unity optical depth. By comparing where the various bins cross the unity optical depth fiducial, we can see good agreement with the location of the peak ionization rates for the 4 bins illustrated in Figure 3. Figure 4 also illustrates how the maximum absorption in each bin is separated by roughly 4–6 km. The exceptions are the two shortest wavelength bins which encompass a larger photon energy range (and hence greater change in the N_2 absorption cross section). Following the same approach as SQ05, the ratio of the photoelectron to photoionization (p_e/p_i) given for each bin in Table 2 is taken at the altitude of unity optical depth. Tables 3 and 4 give similar information for O_2 and O, respectively. Note, there is other information provided in the original SQ05 tables; for example, branching ratios and excited state yields. In those cases, those values are constant across all the soft X-ray bins of SQ05. For example, the dissociative ionization yield of N_2 is 0.96 for the 0.05–0.4 nm bin and the 0.8–1.8 nm bin. Thus going to higher spectral resolution as we have done here does not add new information. Therefore we simply adopted the SQ05 numbers for our 12 bin extension.

Finally, Figure 5 compares the resulting total N_2 ionization rate profiles for our 46 bin model with the SQ05 37 bin model. As with Figure 3, the solar flux comes from FISM for the peak of the Sept 10, 2017 flare; the assumed N_2 profile comes from NRLMSIS2.0 (Emmert et al., 2021). The upper left panel shows the total (assuming overhead sun). It can be seen that the 46 bin model extends the ionization to much lower altitudes than the SQ05 model. This is due to the explicit resolution of very short wavelengths where the N_2 absorption cross section is

SISKIND ET AL. 6 of 19

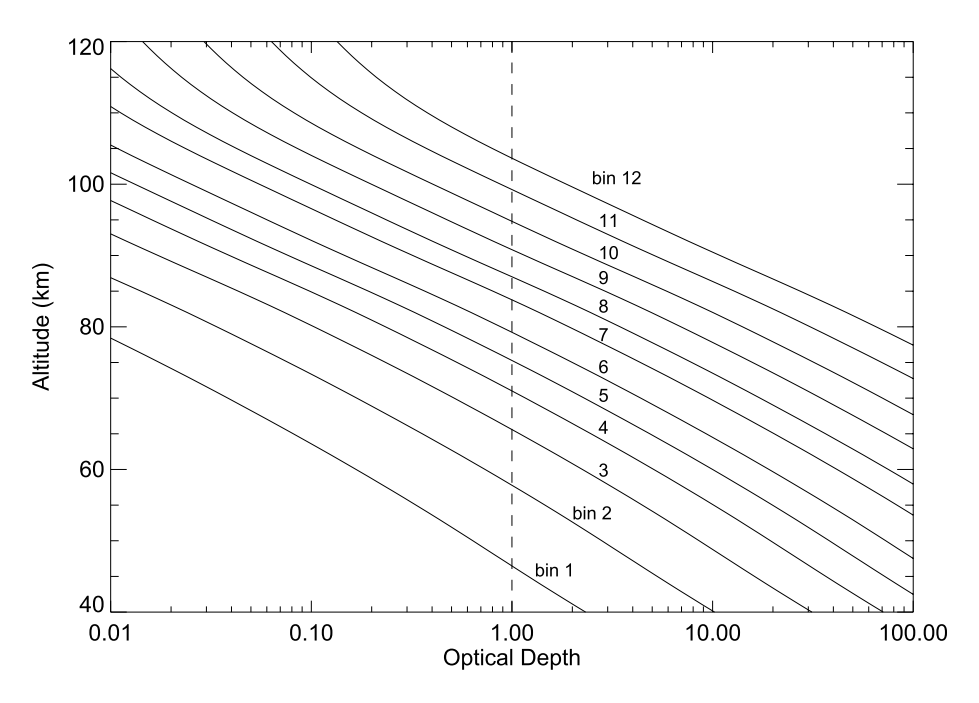


Figure 4. Calculated optical depth for photon absorption for each of the 12 wavelength bins and absorption cross sections presented in Table 1. Overhead sun is assumed. The altitude where each of the curves intersect the vertical dashed line serves as a marker for the altitude of maximum ionization for each bin.

less than 2×10^{-21} cm²s⁻¹. By contrast, the mean cross section given for the first SQ05 bin is 2.5×10^{-21} cm² which corresponds to peak absorption much higher up in the mesosphere, nearer 80 km. Thus our new model is better suited for modeling ionization in the lowermost mesosphere that could be detected, for example, by VLF propagation. It is also worth comparing these ionization rates with those presented by Siskind et al. (2015) for a near overhead sun conditions for much lower (sub C class) X-ray fluxes for 20 September 2004. The model used by Siskind et al. (2015) could not properly account for soft X-rays. Rather, they show that the ionization rate at

Table 3 *Cross Sections and Photoelectron Factors for O*₂

bin no.	λ short, nm	λ long, nm	$\sigma_{abs}\mathrm{cm}^2$	p_e/p_i total		
First SQ05 band (0.05–0.4 nm)						
1	0.05	0.1	6.21×10^{-23}	332.9		
2	0.1	0.15	2.73×10^{-22}	186.2		
3	0.15	0.2	8.32×10^{-22}	130.6		
4	0.2	0.25	1.87×10^{-21}	101.1		
5	0.25	0.3	3.66×10^{-21}	82.6		
6	0.30	0.4	6.94×10^{-21}	66.1		
Second SQ05 band (0.4–0.8 nm)						
7	0.4	0.5	1.50×10^{-21}	51.4		
8	0.5	0.6	2.66×10^{-20}	42.3		
9	0.6	0.8	5.25×10^{-20}	34.0		
Third SQ05 band (0.8–1.8 nm)						
10	0.8	1.0	1.05×10^{-19}	26.4		
11	1.0	1.4	2.25×10^{-19}	20.2		
12	1.4	1.8	4.71×10^{-19}	15.0		

60 km for the tropics is mainly due to galactic cosmic rates at 60 km, with a value about $0.01 \text{ cm}^{-3} \text{ s}^{-1}$, or about a factor of 10^4 lower than calculated here with the 46 bin model for the X9 flare.

The other three panels break out each of our new sub-bins and compare the calculated ionization, both for the new sub-bins and then for the total, with the original coarser SQ05 bin. The progression for the ionization to maximize at lower altitudes as the wavelength gets shorter is clearly seen. Thus the 0.8–1.8 nm bin peaks around 105–110 km, the 0.4–0.8 nm peaks between 90 and 100 km and the 0.05-0.4 nm has a broad peak centered at 80 km, but extending down to below 50 km. As noted above, in all cases, but most notably for the 0.05-0.4 nm bin, our ionization extends to lower altitudes than SQ05. One can also notice a tendency for our total ionization over the sub-bins (the red curves) to be somewhat less than what is obtained with the original SQ05 parameterization, even after accounting for the redistribution with altitude. This is a small effect (≤10%) at E region altitudes, but for the shortest wavelength bin, is quite noticeable. We attribute this difference to lower values for the photoelectron ionization enhancement that we calculate as compared with the mean values given by SQ05. Thus, for the 0.05-0.4 nm bin, SQ05 give a value of 343 for p_i/p_i whereas most of our numbers are significantly less, on average closer to 200. The only values above 300 that would be comparable to the SQ05 value are for the two sub-bins for wavelengths less than 0.15 nm which penetrate to the 50-60 km range. At

SISKIND ET AL. 7 of 19



Table 4	
Cross Sections and Photoelectron F	actors for O

Cross Sections and I notociceiron I detors for O						
bin no.	λ short, nm	λ long, nm	$\sigma_{abs} \mathrm{cm}^2$	p_e/p_i total		
First SQ05 band (0.05–0.4 nm)						
1	0.05	0.1	3.1×10^{-23}	-		
2	0.1	0.15	1.4×10^{-22}	212.7		
3	0.15	0.2	4.2×10^{-22}	149.3		
4	0.2	0.25	9.3×10^{-22}	115.6		
5	0.25	0.3	1.8×10^{-21}	94.5		
6	0.30	0.4	3.5×10^{-21}	75.6		
Second SQ05 band (0.4–0.8 nm)						
7	0.4	0.5	7.5×10^{-21}	58.8		
8	0.5	0.6	1.3×10^{-20}	48.3		
9	0.6	0.8	2.6×10^{-20}	38.9		
Third SQ05 band (0.8–1.8 nm)						
10	0.8	1.0	5.2×10^{-20}	30.2		
11	1.0	1.4	1.1×10^{-19}	23.2		
12	1.4	1.8	2.4×10^{-19}	17.3		

these wavelengths the absolute photon flux from the sun is relatively small, even during a flare.

2.3. TIME-GCM

The first atmospheric model that we use to study the ionospheric flare response is the NCAR TIME-GCM. The TIME-GCM is one of several NCAR global general circulation models of the middle and upper atmosphere. It self-consistently (Roble & Ridley, 1994) solves the momentum, continuity and electrodynamics equations from first principles for the global circulation, temperature, composition and electrodynamics of the mesosphere, thermosphere, and ionosphere. The grid uses spherical coordinates in longitude and latitude and log pressure in the vertical, assuming hydrostatic balance. The resolution of the model is $2.5^{\circ} \times 2.5^{\circ}$ (long x lat) and 4 grids points per vertical scale height, extending from 12 to 4.6×10^{-10} hPa (or about 30 to 450-600 km, depending upon solar activity). The TIE-GCM (Thermosphere Ionosphere Electrodynamics General Circulation Model) that was used by Qian et al. (2019) can be considered as a subset of the TIME-GCM. Both the TIME-GCM and TIE-GCM use a similar EUV/soft X-ray radiative scheme that relies on the SQ05 parameterization. As noted above, we substituted 12 new wavelength bins for the 3 shortest wavelength SQ05 bins.

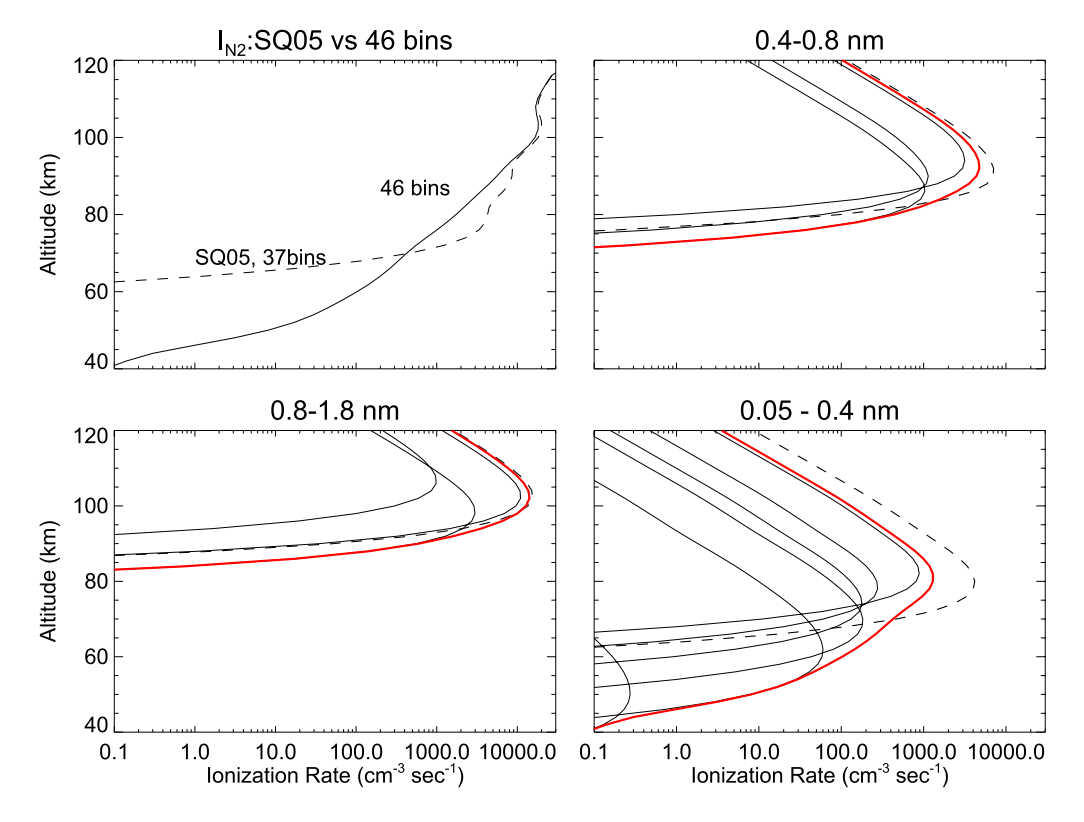


Figure 5. Calculated N_2 ionization rate profiles to compare the sub-bins in Table 1 (46 bin model) with only using the lower resolution wavelength bin of Solomon and Qian (2005) (37 bin model). The upper left hand panel gives the total integrated ionization using the solar spectrum shown in the middle row of Figure 1 (i.e., Sept 10, 2017 for min = 966) for overhead sun conditions. The other three panels break out each of the three shortest wavelength bins of SQ05 and compare with our 12 new sub-bins. In each of these panels, the solid curves are for the individual sub bins within the indicated wavelength range, thus 3 each for the 0.8-1.8 nm and 0.4-0.8 nm bins and 6 for the 0.05-0.4 bin. The thick red curve is the sum over these sub bins. The dashed curve is what is predicted from the original low resolution SQ05 model.

SISKIND ET AL. 8 of 19

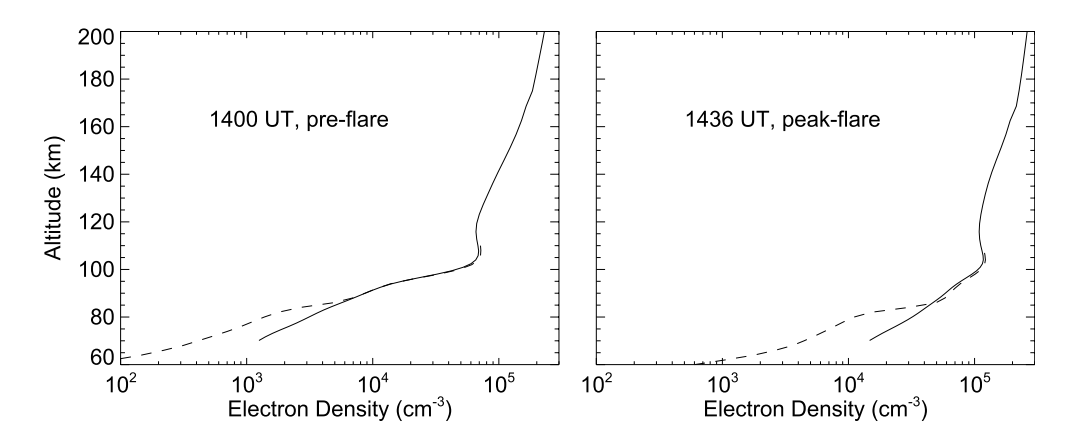


Figure 6. Comparison of calculated electron densities from the TIME-GCM (solid) and the OASIS D region model (dashed) for two times on 7 September 2017. The left panel is prior to the X1.3 flare and right panel is at the peak of the flare. The OASIS model only extends up to 110 km thus the dashed line stops there. Both models use a solar spectrum from FISM (see text).

We have performed two sets of TIME-GCM simulations for the September 2005 and 2017 flare events. For both these simulations, we initialized the model on August 29th to allow for a "spin up" of the model dynamics, electrodynamics, constituents and temperatures. The model was then run out for the three dates for which spectra were presented in Figure 1 with output saved every minute. Two sets of runs were performed for both 2005 and 2017, one which used a pure FISM spectrum at all wavelengths and the second uses a hybrid solar model where we use FISM for EUV wavelengths and NRLFLARE for soft X-ray wavelengths. The rationale for this approach is that at soft X-ray wavelengths, there is less information on the shape of the solar spectrum to constrain the FISM empirical model. At the same time, we expect NRLFLARE to be most accurate for the hot (>10⁶°K) emission lines that characterize the soft X-rays. The interface between the EUV (FISM) and soft X-rays (NRLFLARE) is generally taken to be 2 nm. However, we also explore a scenario where we use NRLFLARE out to 7 nm as per the spectra shown in Figure 1. Note that for the daily averaged background, such as for pre-flare conditions, we only use FISM. As we discuss below, a comparison of the calculated ionosphere using these two solar models with observations highlight which specific wavelengths in the solar spectrum need to be better understood for modeling the effects of flares on the atmosphere.

2.4. OASIS

The other atmospheric model we use is the OASIS (the Originally Austrian model of the IonoSphere) model. OASIS was first described by Torkar and Friedrich (1983) and Gumbel et al. (2003) and recently used by Siskind et al. (2015), (2017) and (2018). Here we have modified OASIS to use the SQ05 ionization parameterization with our new 12 short wavelength bins The need for a D region photochemical model can be seen in Figure 6 which compares the calculated electron density output of the TIME-GCM with that from OASIS with the TIME-GCM for the peak of the 7 September, 2017 X1.3 flare. Here both TIME-GCM and OASIS use the FISM spectrum. Note the excellent agreement from about 85–100 km. This is particularly satisfying given that both models do not use the same neutral atmosphere. OASIS used neutral constituents from NRLMSIS 2.0 (Emmert et al., 2021) while TIME-GCM used neutral inputs from its own calculation. The nitric oxide input into OASIS was taken from TIME-GCM output for this period. But overall the D region electron density during a flare is less sensitive to neutral inputs and more sensitive to solar inputs, which are identical for the two calculations.

Below about 85 km, the two calculated electron density profiles diverge significantly. This is because below 85 km, the ion composition becomes dominated by molecular clusters and proton hydrates which recombine significantly faster than the lighter molecular ions, O_2^+ and NO^+ , which dominate in the upper D and lower E region. For example, at 86 km, 97% of the molecules are O_2^+ and NO^+ , with average recombination rates of $2-4 \times 10^{-7}$ cm³ s⁻¹. By contrast, at 80 km, less than half the ions are O_2^+ and NO^+ and over 30% of the molecules are proton hydrates of the form $H^+(H_2O)n$, n = 1-4 which have recombination rates near 3×10^{-6} cm³ s⁻¹ (Pavlov, 2014), about 10X faster than for O_2^+ and NO^+ . There is some sensitivity of the above fractions to the assumed water vapor profile between 80 and 86 km, for which there is limited data. We use a profile

SISKIND ET AL. 9 of 19



that is consistent with some measurements made by the Solar Occultation for Ice Experiment (SOFIE; Rong et al., 2010) when it sampled low to mid latitudes (cf. Siskind et al., 2019) and which assumes a value for H₂O at 80 km of 2 ppmv. If we used a more extreme value of H₂O, such as that seen in the high latitude summer, with a value of 6 ppmv at 80 km, the electron density at 80 km would be reduced by about 15% due to the greater abundance of proton hydrates. This difference is small compared to the difference between OASIS and TIME-GCM below 85 km. In any event, this added chemistry is not in the TIME-GCM, and the TIME-GCM significantly overestimates the electron density profile at these altitudes. Figure 6 therefore serves to establish the bottom valid altitude for the TIME-GCM electron density calculation as well as demonstrate the need for our subsequent use of OASIS for HF absorption calculations to be described below.

2.5. Mo.Jo

The final component to our suite of models is MoJo (Modernized Jones code), the HF ray-tracing and absorption model. As recently discussed by Zawdie et al. (2017), MoJo solves the range dependent ray-trace equations of Haselgrove and Haselgrove (1960) in spherical coordinates. It uses the Appleton-Hartree dispersion relation with collisions and an external magnetic field, and is based upon the classic Jones and Stephenson (1975) ray-trace code. The ionospheric absorption (in decibels) is defined in Davies (1990):

$$L_a = -8.68 \int k \chi ds \tag{1}$$

where k is the wavenumber, χ the imaginary part of the reflective index and ds is the differential path length. The expression for the absorption coefficient χ is

$$\chi = \frac{e^2}{2m_e c \epsilon_0} \frac{1}{\mu} \frac{N_e v_m}{v_m^2 + (\omega \pm \omega_b \cos \theta)^2}$$
 (2)

where is e is electric charge, m_e the electron mass, e the speed of light, e_0 the electric permittivity of free space, e the real part of the refractive index, e the electron density, e is the angular frequency of the wave, e is the electron gyrofrequency, e the angle between the phase propagation direction and the magnetic field vector, and e is the momentum-transfer collision frequency (e.g., Beharrell & Honary, 2008). MoJo assumes e where e is the sum of the temperature and composition dependent electron-neutral e and electron-ion e collision frequencies, representative of the average over the electron energy distribution function from Schunk and Nagy (1978, 2009). A recent application of MoJo to calculate atmospheric absorption of HF radiowave using electron density profiles from the OASIS model was presented by Siskind et al. (2017).

3. Model-Data Comparisons

3.1. The E Region: Comparison With Incoherent Scatter Radar

To test our photoelectron parameterization, we have compared TIME-GCM calculations for two solar flares, the 10 September 2017 flare and the 7 September 2005 flare with electron density profiles obtained from the Millstone Hill incoherent scatter radar (ISR) situated in Westford, MA, USA (42.6°N, 71.5°W). Both these events have been the subject of much recent study: the 2017 event by Redmon et al. (2018), Qian et al. (2019, 2020), Zhang et al. (2019) and Amaechi et al. (2021), and the 2005 event by Xiong et al. (2011) and Pettit et al. (2018). Qian et al. performed model data comparisons with the SQ05 model and the TIE-GCM. While Xiong et al. (2011) presented the Millstone ISR data for the 2005 event and while Pettit et al. (2018) performed model calculations, to our knowledge, our study here is the first model/ISR comparison for the 2005 flare.

Figure 7 shows the time evolution of the ISR data at 101 km (the lowest altitude with reliable data) for both flares compared with several TIME-GCM calculations which use different solar flux models. To compare with the ISR data, the TIME-GCM was sampled at the nearest model point (41.25 N, 70W) to Westford MA. The dashed curve in each panel uses purely FISM with a peak spectrum as seen in Figures 1 and 2. The solid curve uses the hybrid model described in Section 2.3 above; FISM for wavelengths longer than 2 nm and NRLFLARE for 0.1–2 nm. Finally, the dotted curve uses a hybrid model where FISM is used only for wavelengths longer than 7 nm and NRLFLARE is used for 0.1–7 nm. The use of these different models allows us to evaluate the sensitivity of our

SISKIND ET AL. 10 of 19

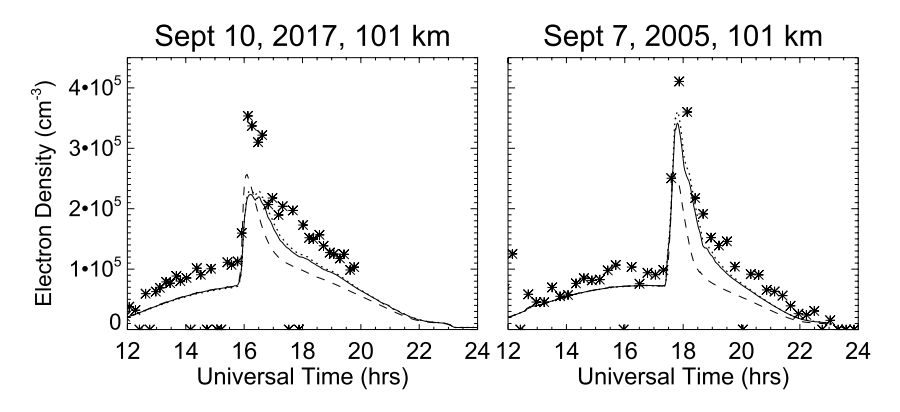


Figure 7. Comparison of incoherent scatter radar data from Millstone Hill with 3 TIME-GCM simulations for the 10 September 2017 X8.3 flare (left panel) and the 7 September 2005 X17 flare (right panel). The stars are the data. The dashed line in each panel is the TIME-GCM using a pure FISM solar spectrum, the solid line uses a hybrid solar spectrum consisting of NRLFLARE for wavelengths less than 2 nm and FISM for wavelengths greater than 2 nm. The dotted line is with a hybrid solar spectrum which uses NRLFLARE out to 7 nm, and FISM for the longer wavelengths.

results to different assumptions about the soft X-ray solar flux. Note that EUV wavelengths longer than 7 nm are not expected to be relevant for ionization at 101 km, except for $\rm O_2$ ionization from Lyman beta at 102.6 nm. According to FISM, the Lyman beta flux only varies by 10%–15% during flares and is included in the above calculations. As expected from Figure 1, the hybrid models with NRLFLARE produce more ionization and yield a greater electron density. The figure shows that using NRLFLARE produces better general agreement than with pure FISM, although the model still underestimates the electron density, by perhaps 20%–25% for the 2005 event and up to 50% for the 2017 event.

Figure 8 compares the altitude profiles of the ISR data for the peak of the respective flares with the model calculations discussed above. The effect of adding the higher flux from NRLFLARE in the 3.2–7.0 nm bin improves the agreement at all altitudes, but again, most notably for the 2005 event. It is clear that the model underestimate of the data persists up to 200 km. This is difficult to explain; however, we do not think it is due to an inadequacy in our solar flare modeling. First, the region of the solar spectrum that produces ionization above 120 km is the EUV which is both better measured and less dependent upon photoelectrons. In addition, as seen in Figure 7, the model underestimate of the ISR data, particularly for the 2017 event, is present prior to the flare onset. Assuming that there is no bias in the ISR data, this suggests other factors, such as neutral composition, or atmospheric cross sections (see Siskind et al., 2019 for a discussion).

3.2. Calculating HF Absorption in the Upper D and Lower E Regions

Our second test of our flare model is in calculating the absorption of HF radiowave. Our motivation for this is the recent paper by Levine et al. (2019) who presented ionosonde data for the September 2017 period (see their

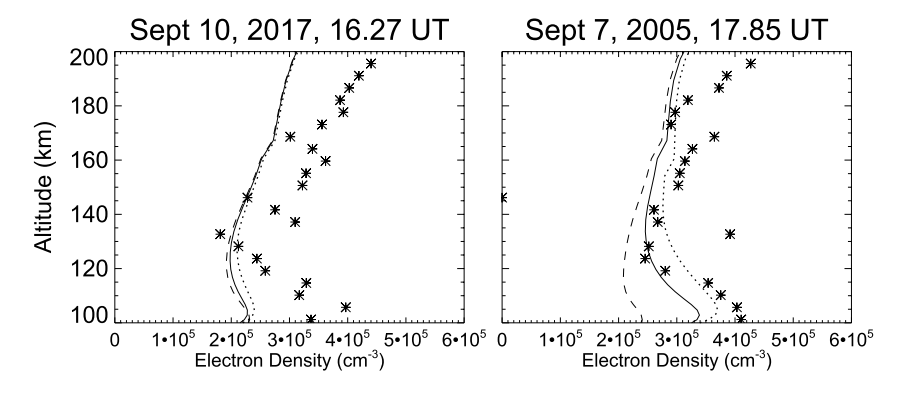


Figure 8. Same comparison as in Figure 7 but in this case, altitude profiles of the ISR data and the three model outputs are shown for the indicated times.

SISKIND ET AL.

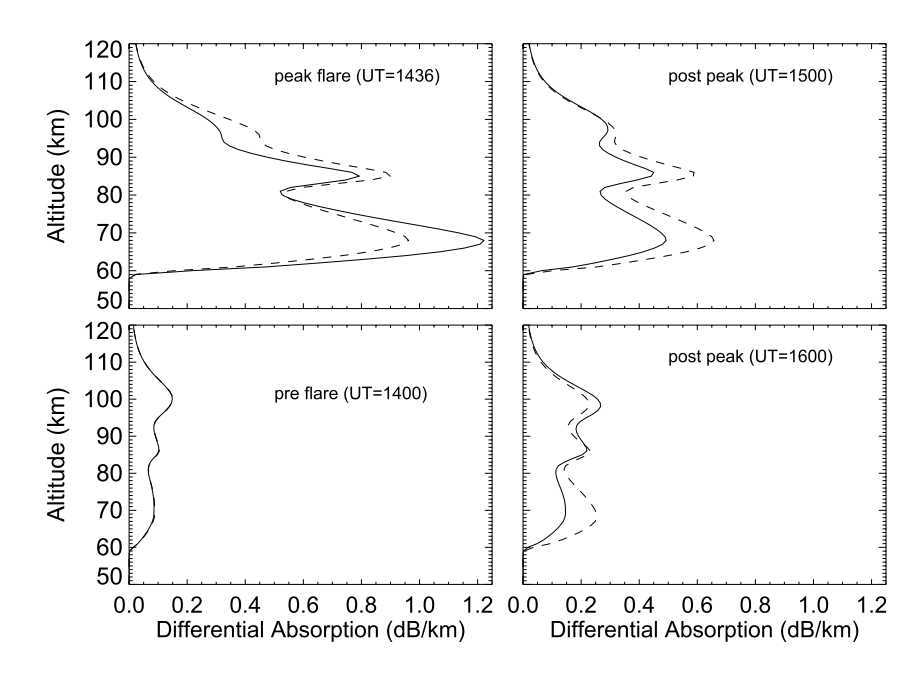


Figure 9. Calculated altitude profiles of differential absorption for 4 times associated with the 7 September 2017 X1.3 flare (see Table 1) for an ionosonde in upstate New York/Western Massachusetts USA (see text). The electron densities are based upon those shown in Figure 6 (see associated text discussion). The solid profiles used the hybrid NRLFLARE/FISM solar spectrum; the dashed used the pure FISM spectrum.

Figures 4 and 5) and compared it with their parameterized D and E region ionosphere model. Here we use the merged OASIS/TIME-GCM profiles as illustrated in Figure 6 to calculate the O-mode absorption with Mojo for the same 357 km E-W path (Bedford NY to Stockbridge MA) presented by Levine et al. (2019). Note, we did have to scale the E and F1 electron densities upward by 35% to get the 6.4 MHz signal to reflect (specifically before the flare enhancement). This scaling is consistent with the model low bias reported in the comparison with the Millstone ISR data, but does not affect the absorption calculation since the absorption (as shown below) occurs below 100 km.

Figure 9 shows altitude profiles of the resulting differential absorption (upleg and downleg rays are combined) for 6.4 MHz for 4 key times in the evolution of the Sept 7, 2017 X1.3 flare. The increases between 65 and 90 km are

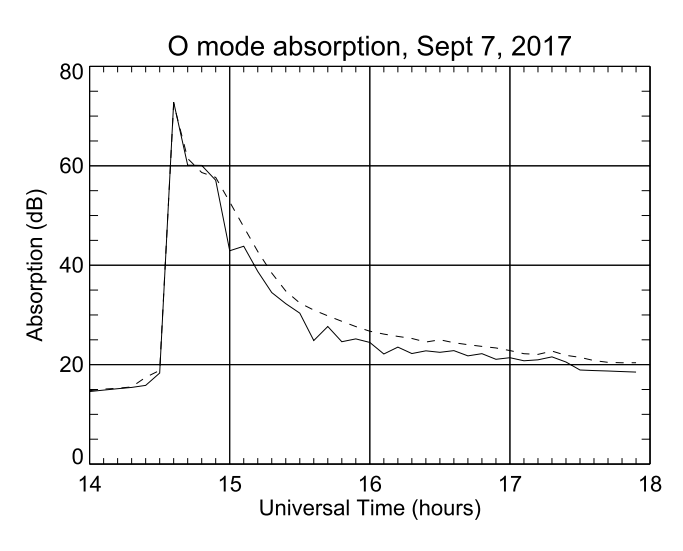


Figure 10. Calculated total absorption as a function of time for the Sept 7, 2017 X1.3 flare shown in Figure 9. The solid line using the hybrid NRLFLARE/FISM model; the dashed uses FISM.

clear. Each panel has two curves-one which used pure FISM as input and one which used the hybrid NRLFLARE/FISM spectrum (except for the 1400 UT, pre-flare case since, as noted above, for daily background we only use FISM). At the flare peak (upper left panel), we can relate the differences in absorption between the FISM-based and NRLFLARE-based calculations back to the differences in predicted photon flux shown in Figure 1. Thus in Figure 1, at wavelengths less than 0.4 nm, NRLFLARE predicts more flux than FISM. From Figures 3 and 4 and the wavelength bins defined in Tables 2–4, we see that these wavelengths are absorbed at and below 70 km and indeed the NRLFLARE based calculation predicts more HF absorption at 65–70 km than the FISM based model. Likewise, from 0.6 to 1.0 nm, FISM predicts the larger flux. These wavelengths correspond to Bins 9 and 10 which Figure 4 shows are absorbed near 85–90 km and here again is consistency-the FISM based calculation yields the greater HF absorption.

Ultimately, since total HF absorption is an integrated quantity along the raypath, the overall absorption which results from using the two solar flux models differs by very little. This is shown in Figure 10 which presents the resulting integrated absorption for both solar flux models as a function of time during the period (calculated every 6 min). In general, although not exact, the agreement with the published ionosonde data of Levine et al. (2019, their

SISKIND ET AL. 12 of 19



Figure 5f) is good. At 1500 UT, the models get approximately 25–35 dB more absorption compared with pre flare at 1400 UT, depending upon which spectrum we use. It seems that NRLFLARE decays more quickly than the FISM-based model and is in better agreement at 1600 UT with the Levine et al. (2019) data. Interestingly at the flare peak we calculate much more absorption than Levine; however, at this particular instant there was no data with which to compare. Certainly, both our calculation and Levine et al. agree in producing more absorption than predicted by the NOAA D-rap model (cf. swpc.noaa.gov/products/d-region-absorption-predictions-d-rap; Akmaev et al., 2010) that they present.

3.3. Comparison Against VLF Models of Flares for the Lower D Region

Our third and final test of our flare model is with previous published data of VLF radio propagation. As discussed by Siskind et al. (2018, and references therein), VLF measurements of the lowermost ionosphere have been made for decades as part of US Navy operational communication programs (McRae & Thomson, 2000). As discussed in those references, VLF waves propagate in a waveguide that consists of the Earth's surface and the lower D region of the ionosphere. Typically, to model VLF propagation, the electron density profile is categorized according to the height of reflection, H', and a sharpness factor, β , in km⁻¹. By day, for quiet conditions, a typical value for H' is about 71 km. This model was introduced by Wait and Spies (1964) and as we will see, implicitly assumes a log-linear shape to the electron density profile. Siskind et al. (2018) showed that the OASIS model was in good agreement with extant models of VLF electron density profiles for quiet conditions. During solar flares, the increase in ionization in the lower D region translates into a lowering of the VLF waveguide such that H' decreases to below 70 km. There is also an increase in β . By comparison with the ionization rate profiles of the shortest wavelength bins discussed in Section 2.2 above and seen in Figures 3 and 4, we can see that VLF data are sensitive to the higher energy portion of the solar spectrum. For this reason, VLF data are of particular interest for the study of solar flares and there have been numerous studies of the VLF response to solar flares (Bourderba et al., 2016; Singh et al., 2014; Thomson et al., 2005; Zigman et al., 2007). In particular, Thomson et al. (2005) have suggested that during the extreme flare of 4 November 2003, that H' was reduced to as low as 53 km.

Unfortunately, the extant models of the VLF response to flares are in disagreement. This can be most clearly seen in Figure 5 of Singh et al. (2014) who compare their model prediction of H' versus flare intensity with the Thomson et al. (2005) model. In general, the Thomson et al. model shows a more pronounced lowering of the waveguide. Thus for M-class flares, Thomson et al. predict values for H' near 64-65 km, and Singh has values near 68-69 km. For an X1 flare, these become 60 and 67 respectively and for the strongest flare considered by Singh et al., the X6.9 flare of 9 August 2011, they get H' = 65.7 km while Thomson predicts H' to be about 56 km. It is difficult to see how both of these models can be simultaneously correct. More recently, Bouderba et al. (2016) also considered the X6.9 flare of 9 August 2011 and derived a value of 64.1 km for H', that is, closer to Singh et al. than Thomson et al. Finally, Hayes et al. (2017) infer a value of H' to be as low as 63 km for a relatively weak C6.8 flare-for such a weak flare, this is lower than any of the previous estimates, even that of Thomson et al. (2005). The sharpness values, β also disagree between the these models. Thus for the X6.9 flare, Singh et al. predict 0.4783, Bouderba et al. predict 0.465 and Thomson et al. about 0.51 km⁻¹. These predictions (for H') are summarized in the last two columns of Table 1 using the formulae presented in Figure 5 of Singh et al. (2014). As is evident, they consistently differ by about 6-7 km. Note, Bourderba et al. (2016) also looked at the 2011 X6.9 flare and independently obtained H' = 64.08 km. This is in good agreement with the Singh et al. model and almost 8 km higher than predicted from the Thomson et al. model. As we will show, these differences for H', of about 1 scale height for the top of the VLF waveguide, translate into an over of magnitude difference in the inferred electron density at any given altitude.

Figure 11 compares the results from the OASIS model against the predictions from the Singh and Thomson VLF models summarized above. The figure shows altitude profiles of the predicted electron density profiles from OASIS for four of the flares summarized in Table 2. The neutral atmosphere uses NRLMSIS with a representative nitric oxide profile for late summer conditions taken from the TIME-GCM runs performed above. The actual results are insensitive to the adopted NO profile for these conditions because the ionization is dominated by N_2 ionization from the soft X-rays. Model results using both pure FISM and using NRLFLARE for the soft X-rays are shown. The peak flux for both FISM and NRLFLARE given by Table 1 for the 0.1–0.15 nm band which, as shown in Figure 3, produces ionization in the 60–65 km altitude range, is relevant to the discussion here. Also as seen in Columns 6 and 7 of Table 1, NRLFLARE tends to predict 2–4 times greater flux than FISM for this

SISKIND ET AL. 13 of 19

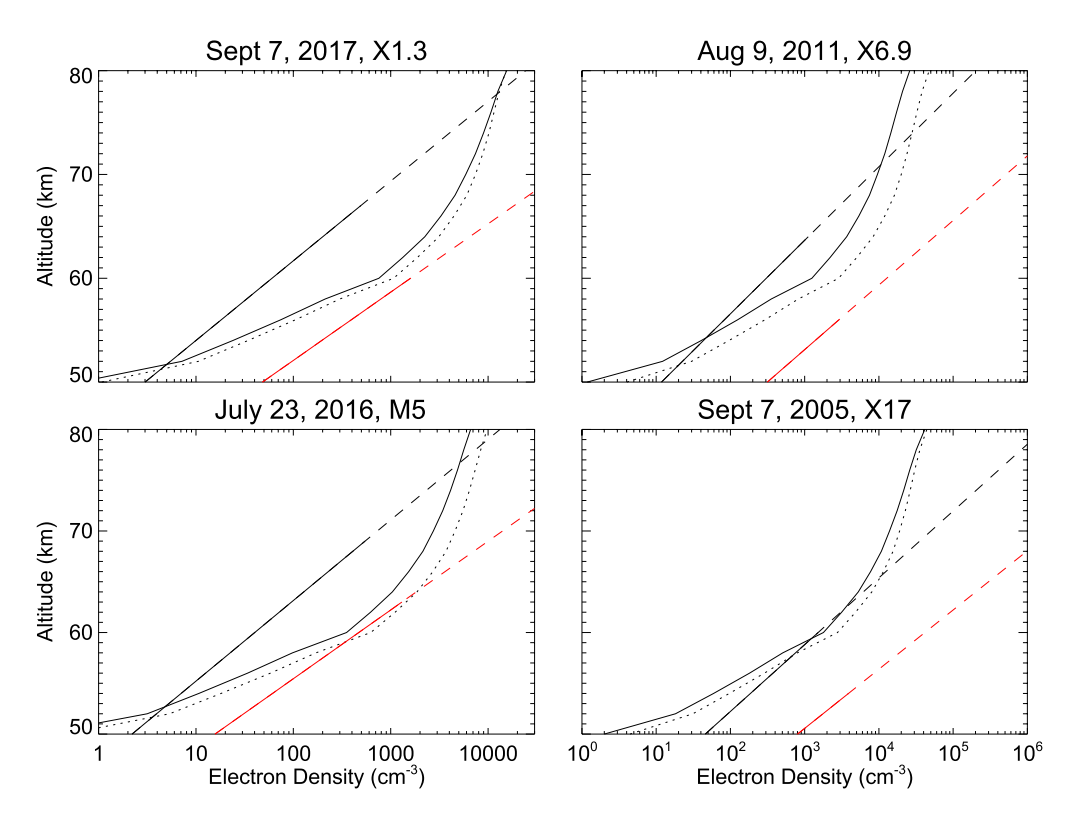


Figure 11. Comparison of two implementations of the OASIS photochemical model (solid and dotted lines) with two VLF-based empirical models of D region electron density response to flares (straight lines). In all 4 four panels, the solid line is OASIS with the solar spectrum from NRLFLARE, the dotted is OASIS with the solar spectrum from FISM. The leftmost (black) straight line is the electron density from the VLF model of Singh et al. (2014); the rightmost (red) line is the electron density from the VLF model of Thomson et al. (2005). These lines are solid up to the altitude representing the top of the waveguide as presented in the rightmost column of Table 1. Above those altitudes they are dashed. All the profiles were calculated for the peak flare times and locations given in Table 1.

band. Both FISM and NRLFLARE are consistent, however, in predicting a factor of 27–28 increase in the solar soft X-ray flux going from the M5 flare to the X17 flare. This increase agrees well, to within 20%–25%, with the change in flare classification in that M5 corresponds to a GOES flux of 5×10^{-5} W/m² and X17 corresponds to a GOES flux of 1.7×10^{-3} W/m², a factor of 34 increase.

While using NRLFLARE predicts electron densities up to 2X greater than using FISM, in general, the differences between the two flavors of the model are small compared with the differences between the predictions from the Singh et al. (2014) and Thomson et al. (2005) models (the rightmost straight red lines in all panels represent the Thomson et al. (2005) model which predicts 10–20X greater [e–] than Singh et al. (2014) model, shown as the leftmost black straight lines). The first difference is that the model lines are not straight on the log-linear graph. This is a key assumption of the Wait and Spies model. The difference is most apparent above the top of the waveguide (marked by the transition from solid to dashed for the VLF lines) where the OASIS model curves away to smaller values. While there are some key assumptions inherent in the OASIS model that we will discuss further, this difference should lend some caution to published VLF-derived electron density results using the Wait and Spies model that extend above the nominal VLF reflection height as represented by H' (e.g., Zigman et al., 2007 (see Table 1 and discussion in text); Basak and Chakrabarti (2013); Bouderba et al. (2016)). It is a reminder that above H', the VLF models are essentially an extrapolation. For this reason, our plot of the VLF profile uses dashed lines to represent the inferred electron density profiles for altitudes above that given by H' in each model.

With that difference in mind, regarding the variation with flare intensity, for the weaker flares (left hand panels), OASIS is closer to the Thomson et al. prediction, particularly in the 60–65 km altitude region which marks the top of the VLF waveguide. However, for the larger flares (right column), the Thomson model greatly exceeds the OASIS model. Below 60 km, the difference is about 2 orders of magnitude. For these flares, the Singh

SISKIND ET AL. 14 of 19

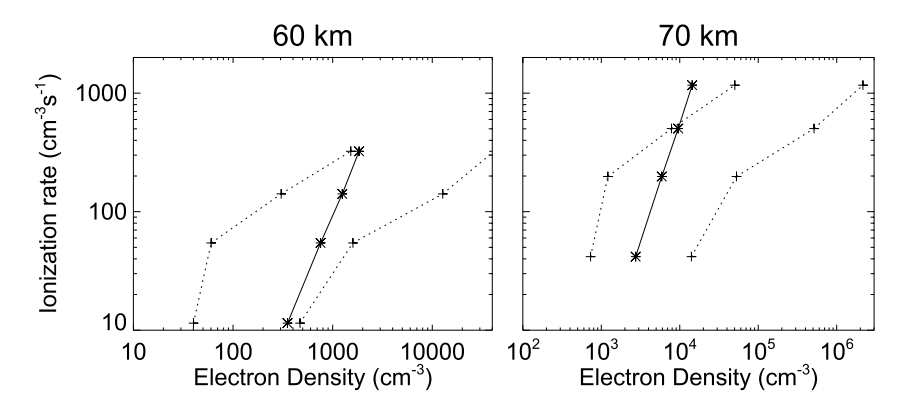


Figure 12. Variation of the peak N_2 ionization rate for the 4 flares shown in Figure 11 versus the resulting electron density at 60 km (left) and 70 km (right). The electron densities are all taken from Figure 11. The solid line with stars is from the OASIS photochemical model, the dashed lines are from the VLF models of Singh et al. (2014) model (leftmost) and the Thomson et al. (2005) model (rightmost).

et al. (2014) model is in better agreement with OASIS. Thus for the X17 event, both OASIS and Singh et al. predict a value of [e-] at 60 km around 1,000 cm⁻³ whereas the Thomson et al. model is around 3×10^4 . Note that in all cases, the VLF models are not as steep as OASIS such that at 50 km, OASIS is always much lower than the VLF models and rapidly increases to within the range of the VLF models by 60 km. This may suggest some interesting areas to explore regarding the possibility of higher energy photons, absorbed near the stratopause, than accounted for in our model.

The pattern indicated in Figure 11, whereby Thomson et al.'s model is in better agreement with OASIS for the weaker flares but Singh et al. agree better for the stronger flares, reflects a much greater increase in predicted [e-] with flare intensity by both of the VLF models than by OASIS. Figure 12 shows this explicitly by plotting the calculated N₂ ionization rate at 60 km versus the resultant model [e-]. As noted earlier, OASIS predicts about a factor of 28 increase the ionization rate which is roughly consistent with the change in GOES flux reflected in the flare classifications in Table 2. The resultant electron density change is about a factor of 5–6 which is broadly consistent with the square root of the ionizing flux and which is a general principle of photochemical models of the ionosphere (Appleton & Piggott, 1954; Palit et al., 2015 and references therein). By contrast, the VLF models predict a relationship between the ionization rate and the electron density which is near, or even exceeds one-to-one. Thus the Singh et al. [e-] varies from 40 cm⁻³ to about 1,500 cm⁻³, or about a factor of 37.5, which is more than the absolute ionization rate change and 5–6 times the OASIS calculated [e-] change. The Thomson et al. model predicts an even greater change, from 470 cm⁻³ to 41,000 cm⁻³, or about a factor of 87.

There are a couple of limitations to our model that need to be considered in this context. First, OASIS is configured to be a steady state model whereas numerous studies of flares have suggested that the time dependence is an important factor in governing the recombination rate (Basak & Chakrabarti, 2013; Chakraborty et al., 2021; Palit et al., 2015; Zigman et al., 2007). Essentially the idea is that the solar irradiance peaks while the ionospheric chemistry lags in its response. Thus the initial ion production is concentrated on the simple molecular ions which recombine much more slowly than the proton hydrates, leading to an enhanced electron density. However, it does not appear that this effect could explain the large difference between the OASIS variation and that inferred by the VLF models. The only photochemical modeling of this varying recombination effect that we are aware of was conducted by Mitra and Rowe (1972). They calculate a factor of 2-5 decrease in the recombination at 70 km during a strong flare. This might suggest a possible 40% to factor of 2 underestimate of the electron density increase by OASIS. While not trivial, it is too small to account for the differences seen in Figure 12. Another uncertainty in the photochemical model is in its representation of negative ion chemistry. As discussed by Torkar and Friedrich (1983), OASIS makes the simplifying assumption that there are only two negative ions, O₂ which rapidly photodetatches, and a second, unspecified negative ion (hereinafter known as X⁻), which photodetatches much more slowly. In principle, if the negative ion composition were to change during a flare, this could alter the model response. We varied the assumed photodetachment rate of X- by a factor of 4, consistent with the difference between the detachment rates of CO₂ and NO₃ (Table 1, Pavlov, 2016) and only got a 25% change in [e-], again not enough to account for the differences between the model variation and inferred observations in

SISKIND ET AL. 15 of 19



Figure 12. Ultimately, we conclude that the differences in interpretation between the different VLF analyses are larger than the uncertainties inherent in our approach using OASIS.

4. Discussion and Conclusions

We have presented a comprehensive flare model, with components that extend from the sun's atmosphere to the Earth's lower ionosphere, which we applied to compare with three datasets covering the D and E regions of the ionosphere. For the E region, our work follows from the studies of Solomon (2006) and Sojka et al. (2014). For both these studies, uncertainties in both photoelectron production and the spectral shape of the soft X-ray solar spectrum were emphasized. By using two different solar spectra and comparing the resultant electron density to ISR data, our results presented here offer better constraints for both these questions. For example, Sojka et al. (2014) assumed that the solar spectrum was "flat" from 1 to 7 nm. Our results from the comparison of NRLFLARE and FISM indicate that this is a good assumption, except in the critical 1–2 nm band that is absorbed near 100 km. Here, the NRLFLARE results suggest an enhancement of the flux which appears consistent with older data from OSO, and we have shown that this improves the TIME-GCM agreement with the ISR data. Clearly, an improved knowledge of the shape of the solar spectrum in the 1–2 nm band is very important for successful modeling of the E region response to solar flares.

Overall, the TIME-GCM simulation of the E region tended to fall somewhat on the low side compared with observations. The differences are not huge, typically in the 25%–50% range, but they seem persistant. Typically the solution has been to scale the soft X-ray flux (cf. Fang et al., 2008; Maute, 2017) since as Solomon (2006) noted, it is hard to imagine what else could be missing "if not soft X-rays." Our results here should provide some constraint as to how much scaling can be applied and still remain consistent with both empirical and theoretical estimates. We note that the TIME-GCM underprediction occurs both before and during the flare and over a relatively broad range of altitudes from 100 to 200 km. Thus while the uncertainty in the 1–2 nm band is important during a flare and for altitudes near 100 km, it is likely insufficient to fully resolve the problem. Moreover, we have noted (Siskind et al., 2019) that there is a risk of over estimating the nitric oxide in the lower thermosphere if the scaling is overdone. We suggest that self-consistent model/data comparisons for both the E region ionosphere and the nitric oxide is an area for future research.

For lower altitudes, the ionospheric D region, we have implemented the solar spectral models and our photoelectron model into the OASIS D region model and compared with published HF absorption and VLF datasets. Clearly a key limitation to our use of OASIS is the fact that it is steady state. This needs to be rectified for future analysis. However, given that OASIS does adequately capture the absorption caused by the X1.3 flare which peaks at 70 km, its not obvious that this is a crippling uncertainly. Our model suggests that for an X17 flare, electron densities at 60 km should peak near 10^3 cm⁻³, which is in agreement with the lowest published VLF estimates for this type of event. Moreover, our analysis clearly shows greater than order of magnitude discrepancies in the derived electron density between published VLF analyses, some of which suggest densities at 60 km reaching greater than 3×10^4 cm⁻³ at 60 km. These discrepancies have not been appreciated in the literature to date; however, we note that very recently, a new VLF analysis approach has been proposed (McCormick & Cohen, 2021) which removes the log-linear assumption inherent in the Wait and Spies (1964) formulation. It would be very interesting to apply this new analysis to solar flares. Until these uncertainties in the VLF-derived electron density profiles are reconciled, we argue that it is premature to draw firm conclusions from the comparison of the VLF data with theoretical models such as OASIS.

Data Availability Statement

FISM was accessed at https://lasp.colorado.edu/lisird. The VA Tech photoelectron model can be found at https://github.com/baileygroup-vt under ACE-PE (Atmospheric Chemistry and Energetics- PhotoElectrons). The TIME-GCM is available from the High Altitude Observatory at the National Center for Atmospheric Research (www.hao.ucar.edu/modeling). Model output, including output from NRLFLARE, processed solar spectra into 46 bin input files, the minute-by-minute TIME-GCM output for the X17, X8.3 and X1.3 flares in Table 1 are all available as python-readable IDL save files on https://map.nrl.navy.mil/map/pub/nrl/flare. The complete MoJo results are also available in a subdirectory in netcdf format. The OASIS model is available at https://github.com/

SISKIND ET AL. 16 of 19



USNavalResearchLaboratory/oasis. The Millstone HIll ISR data used in this study were obtained from the Madrigal database (http://openmadrigal.org).

Acknowledgments

This work was funded by the the NASA Living with a Star (LWS) program. In addition, S.S. at VA Tech was supported in part by NASA Grant 80NSSC19K0815. The Millstone Hill ISR observation and Madrigal database system are provided to the community by MIT Haystack Observatory under NSF grant AGS-1952737 support. Research at MIT was partially supported by NASA Grant 80NSSC19K0078 and MURI grant FA9559-16-1-0364.

References

- Akmaev, R., Newman, A., Codrescu, M., Schulz, C., & Nerney, E. (2010). D-RAP model validation: Scientific report. Retrieved from https://www.ngdc.noaa.gov/stp/drap/DRAP-V-Report1.pdf
- Amaechi, P. O., Akala, A. O., Oyedokun, J. O., Simi, K. G., Aghogho, O., & Oyeyemi, E. O. (2021). Multi-instrument investigation of the impact of the space weather events of 6-10 September 2017 (Vol. 19). Space Weather. e2021SW002806. https://doi.org/10.1029/2021SW002806
- Appleton, E., & Piggott, W. R. (1954). Ionospheric absorption measurements during a sunspot cycle. *Journal of Atmospheric and Terrestrial Physics*, 5(1–6), 141–172. https://doi.org/10.1016/0021-9169(54)90029-x
- Bailey, S. M., Barth, C. A., & Solomon, S. C. (2002). A model of nitric oxide in the lower thermosphere. *Journal of Geophysical Research*, 107(A8), 1205. https://doi.org/10.1029/2001JA000258
- Basak, T., & Chakrabarti, S. K. (2013). Effective recombination coefficient and solar zenith angle effects on low-latitude D-region ionosphere evaluated from VLF signal amplitude and its time delay during X-ray solar flares. Astrophysics and Space Science, 348(2), 315–326. https://doi.org/10.1007/s10509-013-1597-9
- Beharrell, M., & Honary, F. (2008). A new method for deducing the effective collision frequency profile in the D-region. *Journal of Geophysical Research*, 113(A5), A05303. https://doi.org/10.1029/2007JA012650
- Bouderba, Y., NaitAmor, S., & Tribeche, M. (2016). Study of the solar flares effect on VLF radio signal propagating along NRL-ALG path using LWPC code. *Journal of Geophysical Research*, 121(7), 6799–6807. https://doi.org/10.1002/2015JA022233
- Chakraborty, S., Ruohoniemi, J. M., Baker, J. B. H., Fiori, R. A. D., Bailey, S. M., & Zawdie, K. A. (2021). Ionospheric sluggishness: A characteristic time-lag of the ionospheric response to solar flares. *Journal of Geophysical Research*, 126(4). https://doi.org/10.1029/2020JA028813
- Chamberlin, P. C., Eparvier, F. G., Knoer, V., Leise, H., Pankratz, A., Snow, M., et al. (2020). The flare irradiance spectral model-version 2(FISM2). Space Weather, 18(12), e2020SW002588. https://doi.org/10.1029/2020SW002588
- Chamberlin, P. C., Woods, T. N., & Eparview, F. G. (2008). Flare irradiance spectral model (FISM): Flare component algorithms and results. Space Weather, 6(5), S05001. https://doi.org/10.1029/2007SW000372
- Curto, J. J., Amory-Mazaudier, C., Torta, J. M., & Menvielle, M. (1994). Solar flare effects at Ebre: Unidimensional physical, integrated model. Journal of Geophysical Research, 99(A12), 23289–23296. https://doi.org/10.1029/93ja02270
- Davies, K. (1990). Ionospheric radio. The Institution of Engineering and Technology.
- DelZanna, G., Dere, K. P., Young, P. R., & Landi, E. (2021). CHIANTI- an atomic database for emission lines, XVI. Version 10, Further extensions. The Astrophysical Journal, 909(1), 38. https://doi.org/10.3847/1538-4357/abd8ce
- Dere, K. P., Landi, E., Mason, H. E., Monsignori Fossi, B. C., & Young, P. R. (1997). CHIANTI- an atomic database for emission lines, i. Astronomy & Astrophysics Supplement Series, 125(1), 149–173. https://doi.org/10.1051/aas:1997368
- Eccles, J. V., Hunsucker, R. D., Rice, D., & Sojka, J. J. (2005). Space weather effects on midlatitude HF propagation paths: Observations and a data-driven D region model. Space Weather, 3(1), S01002. https://doi.org/10.1029/2004SW000094
- Emmert, J. T., Drob, D. P., Picone, J. M., Siskind, D. E., Jones, M., Mlynczak, M. G., et al. (2021). NRLMSIS 2.0 A whole atmosphere empirical model. *Earth and Space Science*, 7(3). https://doi.org/10.1029/2020EA001321
- Fang, T. W., Richmond, A. D., Liu, J. Y., Maute, A., Lin, C. H., Chen, C. H., & Harper, B. (2008). Model simulation of the equatorial electroject in the Peruvian and Philippine sectors. *Journal of Atmospheric and Solar-Terrestrial Physics*, 70(17), 2203–221. https://doi.org/10.1016/j.jastp.2008.04.021
- Fuller-Rowell, T. J. (1993). Modeling the solar cycle change in nitric oxide in thermosphere and upper mesosphere. *Journal of Geophysical Research*, 98(A2), 1559–1570. https://doi.org/10.1029/92ja02201
- Grodji, O. D. F., Doumbia, V., Amaechi, P. O., A-Mazaudier, C., N'guessan, K., Diaby, K. A. A., et al. (2022). A study of solar flare effects on the geomagnetic field components during solar cycles 23 and 24. Atmosphere, 13(1), 69. https://doi.org/10.3390/atmos13010069
- Gumbel, J., Siskind, D. E., Witt, G., Torkar, K. M., & Friedrich, M. (2003). Influences of ice particles on the ion chemistry of the polar summer mesosphere. *Journal of Geophysical Research*, 108(D8), 8436. https://doi.org/10.1029/2002JD002413
- Haselgrove, C. B., & Haselgrove, J. (1960). Twisted ray paths in the ionosphere. Proceedings of the Physical Society, London, 75(3), 357–363. https://doi.org/10.1088/0370-1328/75/3/304
- Hayes, L. A., Gallagher, P. T., McCauley, J., Dennis, B. R., Ireland, J., & Inglis, A. (2017). Pulsations in the Earth's lower ionosphere synchronized with solar flare emission: Flaring pulsations detected in D-region. *Journal of Geophysical Research*. 122(10). 9841–9847. https://doi.org/10.1002/2017JA024647
- Henke, B. L., Gullikson, E. M., & Davis, J. C. (1993). X-ray interactions: Photoabsorption, scattering, transmission, and reflection at E=50-30,000 eV, Z=1-92. *Atomic Data and Nuclear Data Tables*, 54(2), 181–342. https://doi.org/10.1006/adnd.1993.1013
- Jones, M., Jr., Emmert, J. T., Drob, D. P., & Siskind, D. E. (2017). Middle atmosphere dynamical sources of the semiannual oscillation in the thermosphere and ionosphere. *Geophysical Research Letters*, 44(1), 12–21. https://doi.org/10.1002/2016GL071741
- Jones, R. M., & Stephenson, J. J. (1975). A versatile three dimensional ray tracing computer program for radio waves in the ionosphere. Technical Report 7625476. Department of Commerce. Office of Telecommunications.
- Kreplin, R., Chubb, T., & Friedman, H. (1962). X-ray and Lyman alpha emission from the sun as measured by the NRL SR-1 satellite. *Journal of Geophysical Research*. 67(6). 2231–2253. https://doi.org/10.1029/jz067i006p02231
- Levine, E. V., Sultan, P. J., & Teig, L. J. (2019). A parameterized model of X-ray solar flare effects on the lower ionosphere and HF propagation. Radio Science, 54(2), 168–180. https://doi.org/10.1029/2018RS006666
- Li, N., Lei, J., Luan, X., Chen, J., Zhong, J., Wu, Q., et al. (2019). Responses of the D region ionosphere to solar flares revealed by MF radar measurements. *Journal of Atmospheric and Solar-Terrestrial Physics*, 182, 211–216. https://doi.org/10.1016/j.jastp.2018.11.014
- Maute, A. (2017). TIEGCM-ICON. Space Science Reviews, 212(1-2), 523-551. https://doi.org/10.1007/s11214-017-0330-3
- McCormick, J. C., & Cohen, M. B. (2021). A new four-parameter D region ionosphere model: Inferences from lightening-emitted VLF signals. *Journal of Geophysical Research*, 126(12). https://doi.org/10.1029/2021JA029849
- McRae, W. M., & Thomson, N. R. (2000). VLF phase and amplitude: Daytime ionospheric parameters. *Journal of Atmospheric and Solar-Ter*restrial Physics, 62(7), 609–618. https://doi.org/10.1016/s1364-6826(00)00027-4
- McRae, W. M., & Thomson, N. R. (2004). Solar flare induced ionospheric D-region enhancements from VLF phase and amplitude observations. Journal of Atmospheric and Solar-Terrestrial Physics, 66(1), 77–87. https://doi.org/10.1016/j.jastp.2003.09.009

SISKIND ET AL. 17 of 19



- Mitra, A. P., & Rowe, J. N. (1972). Ionospheric effects of solar flares, VI. Changes in D region ion chemistry during solar flares. *Journal of Atmospheric and Terrestrial Physics*, 34(5), 795–806. https://doi.org/10.1016/0021-9169(72)90112-2
- Neupert, W. M., Gates, W., Swartz, M., & Young, R. (1967). Observation of the solar flare X-ray emission line spectrum of iron from 1.3 to 20 A. *The Astrophysical Journal*, 149, L79–L83. https://doi.org/10.1086/180061
- Nicolet, M., & Aikin, A. C. (1960). The formation of the D region of the ionosphere. *Journal of Geophysical Research*, 65(5), 1469–1483. https://doi.org/10.1029/jz065i005p01469
- Palit, S., Basak, T., Pal, S., & Chakrabarti, S. K. (2015). Theoretical study of lower ionospheric response to solar flares: Sluggishness of D-region and peak time delay. *Astrophysics and Space Science*, 356(1), 19–28. https://doi.org/10.1007/s10509-014-2190-6
- Pavlov, A. V. (2014). Photochemistry of ions at D-region altitudes of the ionosphere: A review. Surveys in Geophysics, 35(2), 259–334. https://doi.org/10.1007/s10712-013-9253-z
- Pavlov, A. V. (2016). Influence of atmospheric solar radiation absorption on photodestruction of ions at D-region altitudes of the ionosphere. Surveys in Geophysics, 37(4), 811–844. https://doi.org/10.1007/s01712-016-9371-5
- Pettit, J., Randall, C. E., Marsh, D. R., Bardeen, C. G., Qian, L., Jackman, C. H., et al. (2018). Effects of the September 2005 solar flare and solar proton events on the middle atmosphere in WACCM. *Journal of Geophysical Research*, 123(7), 5747–5763. https://doi.org/10.1029/2018JA025294
- Qian, L., Wang, W., Burns, A. G., Chamberlin, P. C., Coster, A., Zhang, S.-R., & Solomon, S. C. (2019). Solar flare and geomagnetic activity effects on the thermosphere and ionosphere during 6-11, Sept 2017. *Journal of Geophysical Research*, 124(3), 2298–2311. https://doi.org/10.1029/2018JA026175
- Qian, L., Wang, W., Burns, A. G., Chamberlin, P. C., & Solomon, S. C. (2020). Responses of the thermosphere and ionosphere system to concurrent solar flares and geomagnetic storms. *Journal of Geophysical Research*, 125(3), https://doi.org/10.1029/2019JA027431
- Redmon, R. J., Seaton, D. B., Steenburgh, J. R., He, J., & Rodriguez, J. V. (2018). September 2017's geoeffective space weather and impacts on Caribbean radio communications during hurricane response. Space Weather, 16(9), 1190–1201. https://doi.org/10.1029/2018SW001897
- Reep, J. W., Siskind, D. E., & Warren, H. P. (2022). Solar flare irradiance scalings: Observations and modeling. The Astrophysical Journal, 927, 103. https://doi.org/10.3847/1538-4357/ac4784
- Reep, J. W., Warren, H. P., Moore, C. S., Suarez, C., & Hayes, L. A. (2020). Simulating solar flare irradiance with multithreaded models of flare arcades. *The Astrophysical Journal*, 895(1), 30. https://doi.org/10.3847/1538-4357/ab89a0
- Reid, G. C. (1977). The production of water cluster positive ions in the quiet time D region. *Planetary and Space Science*, 25(3), 275–290. https://doi.org/10.1016/0032-0633(77)90138-6
- Roble, R. G., & Ridley, E. C. (1994). A thermosphere-ionosphere-mesosphere-electrodynamics general circulation model (TIME-GCM): Equinox solar cycle minimum conditions (30-500 km). Geophysical Research Letters, 21(6), 417–420. https://doi.org/10.1029/93GL03391
- Rong, P. P., Russell, J. M., Gordley, L. L., Hervig, M. E., Deaver, L., Bernath, P. F., & Walker, K. A. (2010). Validation of V1.022 mesospheric water vapor observed by the solar occultation for ice experiment on the aeronomy of ice in the mesosphere satellite. *Journal of Geophysical Research*, 115(D24). https://doi.org/10.1029/2010JD014269
- Schunk, R. W., & Nagy, A. F. (1978). Electron temperatures in the F region of the ionosphere: Theory and observations. *Review of Geophysics*, 16(3), 355–399. https://doi.org/10.1029/RG016i003p00355
- Schunk, R. W., & Nagy, A. F. (2009). Ionospheres: Physics, plasma physics, and chemistry. Cambridge University Press.
- Singh, A. K., Singh, A. K., Singh, R., & Singh, R. P. (2014). Solar flare induced D-region ionospheric perturbations evaluated from VLF measurements. Astrophysics and Space Science, 350, 1–9. https://doi.org/10.1007/s10509-013-1699-4
- Siskind, D. E., Barth, C. A., & Cleary, D. D. (1990). The possible effects of solar soft X-rays on thermospheric nitric oxide. *Journal of Geophysical Research*, 95(A4), 4311–4317. https://doi.org/10.1029/ja095ia04p04311
- Siskind, D. E., Jones, M., Jr., Drob, D. P., McCormack, J. P., Hervig, M. E., Marsh, D. R., et al. (2019). On the relative roles of dynamics and chemistry governing the abundance and diurnal variation of low-latitude thermospheric nitric oxide. *Annals of Geophysics*. 37(1), 37–48. https://doi.org/10.5194/angeo-37-37-2019
- Siskind, D. E., Mlynczak, M. G., Marshall, T., Friedrich, M., & Gumbel, J. (2015). Implications of odd oxygen observations by the TIMED-SABER instrument for D region modeling. *Journal of Atmospheric and Solar-Terrestrial Physics*, 124, 63–70. https://doi.org/10.1016/j.iastp.2015.01.014
- Siskind, D. E., Strickland, D. J., Meier, R. R., Majeed, T., & Eparvier, F. G. (1995). On the relationship between the solar soft X-ray flux and thermospheric nitric oxide: An update with an improved photoelectron model. *Journal of Geophysical Research*, 100(A10), 19687–19694. https://doi.org/10.1029/95ja01609
- Siskind, D. E., Zawdie, K. A., Sassi, F., Drob, D., & Friedrich, M. (2017). Global modeling of the low- and middle-latitude ionospheric D and lower E regions and implications for HF radio wave absorption. Space Weather, 15(1), 115–130. https://doi.org/10.1002/2016SW001546
- Siskind, D. E., Zawdie, K. A., Sassi, F., Drob, D. P., & Friedrich, M. (2018). An intercomparison of VLF and sounding rocket techniques for measuring the daytime D region ionosphere: Theoretical implications. *Journal of Geophysical Research*, 123(10), 8688–8697. https://doi. org/10.1029/2018JA025807
- Sojka, J., Jensen, J., David, M., Schunk, R. W., Woods, T., & Eparvier, F. (2013). Modeling the ionospheric E and F1 regions: Using SDO-EVE. Journal of Geophysical Research, 118(8), 5379–5391. https://doi.org/10.1002/2013jgra.50480
- Sojka, J., Jensen, J. B., David, M., Schunk, R. W., Woods, T., Eparvier, F., et al. (2014). Ionospheric model-observation comparisons: E-Layer at arecibo. *Journal of Geophysical Research*, 119(5), 3844–3856. https://doi.org/10.1002/2013JA019528
- Solomon, S. C. (2006). Numerical models of the E-region ionosphere. Advances in Space Research, 37(5), 1031–1037. https://doi.org/10.1016/j.asr.2005.09.040
- Solomon, S. C., Bailey, S. M., & Woods, T. N. (2001). Effect of solar soft X-rays on the lower ionosphere. Geophysical Research Letters, 28(11), 2149–2152. https://doi.org/10.1029/2001gl012866
- Solomon, S. C., & Qian, L. (2005). Solar extreme ultraviolet irradiance for general circulation models. *Journal of Geophysical Research*, 110(A10), A10306. https://doi.org/10.1029/2005JA011160
- Thomas, L., & Bowman, M. R. (1985). Model studies of the D-region negative-ion composition during dya-time and night-time. *Journal of Atmospheric and Terrestrial Physics*, 47(6), 547–556. https://doi.org/10.1016/0021-9169(85)90037-6
- Thomson, N. R., Rodger, C. J., & Clilverd, M. A. (2005). Large solar flares and their ionospheric D region enhancements. *Journal of Geophysical Research*, 110(A6), A06306. https://doi.org/10.1029/2005JA011008
- Torkar, K. M., & Friedrich, M. (1983). Tests of an ion-chemical model of the D-and lower E-region. *Journal of Atmospheric and Terrestrial Physics*, 45(6), 369–385. https://doi.org/10.1016/s0021-9169(83)81097-6
- Wait, J. R., & Spies, K. P. (1964). Characteristics of the Earth-ionosphere waveguide for VLF radio waves. Natl Bur. of Stand. NBS Tech. Note 300.

SISKIND ET AL. 18 of 19



- Warren, H. P. (2005). A solar minimum irradiance spectrum for wavelengths below 1200 A. *The Astrophysical Journal Supplement Series*, 157(1), 147–173. https://doi.org/10.1086/427171
- Woods, T. N., Bailey, S. M., Peterson, W. K., Solomon, S. C., Warren, H. P., Eparvier, F. G., et al. (2003). Extreme Ultraviolet variability and the terrestrial photoelectron response. *Space Weather*, 1. https://doi.org/10.1029/2003SW000010
- Xiong, G., Weixing, W., Liu, L., Withers, P., Zhao, B., Ning, B., et al. (2011). Ionospheric response to the X-class solar flare on 7 September 2005. Journal of Geophysical Research, 116(A11), A11317. https://doi.org/10.1029/2011JA016961
- Zawdie, K. A., Drob, D., Siskind, D. E., & Coker, C. (2017). Calculating the absorption of HF radiowave in the ionosphere. *Radio Science*, 52(6), 767–783. https://doi.org/10.1002/2017RS006256
- Zhang, S.-R., Coster, A. J., Erickson, P. J., Goncharenko, L. P., Rideout, L. P., & Vierinin, J. (2019). Traveling ionospheric disturbances and ionospheric perturbations associated with solar flares in September 2017. *Journal of Geophysical Research*, 60(8), 895–5917. https://doi.org/10.1029/2019JA026585
- Zigman, V., Grubor, D., & Sulic, D. (2007). D-region electron density evaluated from VLF amplitude time delay during X-ray solar flares. *Journal of Atmospheric and Solar-Terrestrial Physics*, 69(7), 776–792. https://doi.org/10.1016/j.jastp.2007.01.012

SISKIND ET AL. 19 of 19